Phase-Contrast Tomography with X-ray Hartmann wavefront sensor

Ginevra Begani Provinciali[*a,b], Alessia Cedola[b], Ombeline de La Rochefoucauld[c] and Philippe Zeitoun[a]

[a]LOA, ENSTA Paris, CNRS, Ecole Polytechnique IP Paris, 828 Boulevard des Maréchaux, 91120 Palaiseau, France
[b]Institute of Nanotechnology-CNR c/o Physics Department, Sapienza University of Rome, Piazzale Aldo Moro 5, 00185 Rome, Italy
[c]Imagine Optic, rue François Mitterrand, 33400 Talence, France

ABSTRACT

The Hartmann wavefront sensor is able to measure, separately and in absolute, the real δ and imaginary parts β of the X-ray refractive index. While combined with tomographic setup, Hartmann sensor opens many interesting opportunities behind the direct measurement of the material density. In order to handle the different ways of using an X-ray wavefront sensor in imaging, we developed 3D wave propagation model based on Fresnel propagator. The model is made in a way to manage any degree of spatial coherence of the source, thus enabling to model accurately experiments using tabletop source, high harmonic generation, plasma-based soft X-ray laser, synchrotron or X-ray free-electron laser. Beam divergence is described in a physical manner consistent with the spatial coherence.The capabilities of the Hartmann wavefront sensor will be compared with experimental results from in-line X-ray Phase Contrast Tomography.

Keywords: Phase-Contrast Imaging, Hartmann sensor, Tomography, Simulation

1. INTRODUCTION

High resolution and low dose soft tissue imaging is an open challenge in medical imaging. New possibilities for X-ray imaging with micrometer and sub micrometer resolution are now possible thanks to new generation radiation sources, characterized by high coherence and brilliance.

Unlike the classical absorption-based X-ray techniques, phase contrast imaging imposes that the modification of the X-ray wavefront of the beam passing through the sample can be transformed into contrast, and hence reconstructed indirectly by a number of methods. Among these, In-line phase-contrast[1–4] enables weakly absorbing objects to be imaged successfully with X-rays without the use of optics or contrast agents.

A tridimensional reconstruction of the object is crucial to resolve the spatial organization of inner details, in particular for biomedical applications.[5] X-ray tomography provides a volumetric visualization of the specimen applying a reconstruction algorithm on 2D projections acquired at many illumination angles. Thus, X-ray tomography is a 3D high-resolution technique that greatly enhances the visibility of small structure inside the sample.

One of the key challenge of biomedical imaging is to increase image contrast of weakly absorbing materials. Standard X-ray imaging, in fact, can resolve inner details in the sample based on their absorption variations only, making challenging to separate structures with close density values.

In the hard X-ray region, phase contrast is predominant over the absorption contrast enhancing features that are invisible in absorption. Moreover, since light materials are almost transparent to X-rays the dose delivered to the sample is definitely lower than in standard X-ray tomography. The combination of Phase Contrast Imaging with Tomography allows to investigate in all the spatial directions low absorbing samples. Many techniques have been implemented to perform X-ray Phase Contrast Tomography (XPCT) like Free-Space Propagation set-ups,[6,7] Talbot,[8]coded aperture[2] and interferometry.[9]

*Send correspondence to G.B.P.: E-mail: ginevra.begani@ensta-paris.fr

International Conference on X-Ray Lasers 2020, edited by Davide Bleiner,
Proc. of SPIE Vol. 11886, 118860J · © 2021 SPIE · CCC code:
0277-786X/21/$21 · doi: 10.1117/12.2593107

For biological application measuring the density variations inside the tissues is an important parameter to differentiate morphological structures and their changes. Object densities are described by their index of refraction $n(\omega) = 1 - \delta(\omega) - i\beta(\omega)$, where ω is the wave pulsation , $\delta(\omega)$ is proportional to the phase and $\beta(\omega)$ to the absorption. Many Phase Contrast techniques can only provide images where the contribution of phase (δ) and absorption (β) properties of the sample are mixed together.
In particular, in Free-Space Propagation Phase Contrast a phase retrieval algorithm[10] is used to recover the intensity at the object plane making use of the ratio δ/β. A widely used single-material phase-retrieval method was developed by Paganin.[11] In this case it is impossible to separate the contribution of phase and absorption, and therefore to calculate the exact density of the material or its chemical composition.
Here, we present some results obtained by Free-Space Propagation XPCT applied to the study of neurodegenerative diseases. In addition to that, we introduce an alternative phase contrast technique that makes use of the Hartmann wavefront sensor. In this way a direct and separate measurement of phase and absorption can be obtained. Finally, since many structural and experimental parameters need to be optimized, a simulation tool for Hartmann sensor imaging is shown as well as experimental results.

2. RESULTS AND DISCUSSION

2.1 XPCT for the investigation of neurogenerative diseases

The propagation of a coherent/partially coherent X-ray beam interacting with a sample will induce refraction of the X-ray beam from its original path. Therefore, the local change of density in the sample will create small interference fringes that can be detected by placing the detector far from the sample. Being able to differentiate small density changes inside biological tissue, XPCT is particularly appealing for biomedical applications.
The anatomical and physiological similarities between humans and animals, particularly mammals, have prompted researchers to investigate a large range of mechanisms in animal models before applying their discoveries to humans. Genetic mutations have been associated with neurodegenerative diseases onset and animal models that mimic the human disease are widely used in clinical and pre-clinical research. We will present some experimental results, in particular mice models for Amyotrofic Lateral Sclerosis (ALS) and Alzheimer Disease (AD) were investigated in brain and spinal cord samples.
Tracking morphological alterations inside the tissue is crucial for neurodegenerative disease diagnosis and for monitoring disease treatment. XPCT measurements were performed at the ID 17 beamline of European Synchrotron Radiation Facility (ESRF) in Grenoble (France).
Animal experimentation was approved by the Italian Ministry of Health and carried out in agreement with the institutional guidelines and international laws (Directive 2010/63/EU on the protection of animals used for scientific purposes, transposed into the Italian legislation by the 'Decreto Legislativo' of 4 March 2014, n. 26).
For ALS-affected mice spinal cords the monochromatic incident beam was set at 30 keV with a sample-detector distance of 2.3 m and a detector pixel size of 3.06 µm. For AD-affected mice brains the XPCT experiment was performed with monochromatic incident beam set at 48.5 keV with a sample-detector distance of 3 m and a detector pixel size of 3.06 µm.
The tomography data was acquired with 2000 projections covering a total angle range of 360°. Phase retrieval was performed using a single distance method developed by Paganin[11] .
Data pre-processing, phase retrieval and reconstruction were performed using the SYRMEP Tomo Project software[12,13] .
XPCT of mouse brain and spinal cord, affected by AD and ALS respectively, are shown in Fig.1. Morphological changes can be seen in 20 months old mouse brain affected by AD (APP/PS1 model) (Fig.1a). Alzheimer disease (AD) is a progressive neurodegenerative disorder that gradually robs the patient of cognitive function implying a type of memory defect with difficulty in learning and recalling new information[14] .
The occurrence of AD is connected with the presence of neuritic plaques and neurofibrillary tangles inside the brain. The abnormal over-expression of proteins (amyloid and tau) in and around brain cells will lead to the formation of deposits called plaques.
Significantly increasing in amyloid deposition is strictly connected with brain aging. In Fig. 1a a late stage AD brain is shown, where the plaques are concentrated in the inner part of the Hippocampus (upper inset) as well as in the brain cortex (lower inset). Thanks to the high contrast provided by XPCT brain fibers entering the

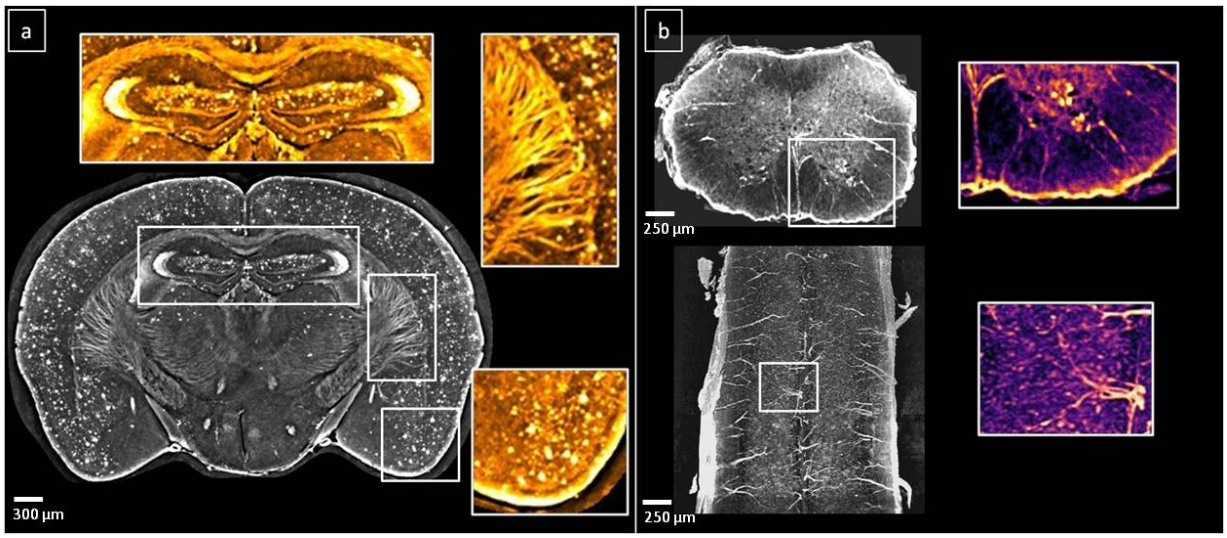

Figure 1. XRPCT of mouse brain and spinal cord. a) 20 months old mouse brain affected by Alzheimer disease(APP/PS1 model). A large number of amyloid plaques can be seen in the brain tissue (white spots). The plaques are concentrated in the inner part of the Hippocampus (upper inset) as well as in the brain cortex (lower inset). Thanks to the high contrast provided by XPCT brain fibers entering the cortex can be clearly resolved (right top inset). b) 60 days old mouse spinal cord affected by ALS (SOD1 model). In the spinal cord transverse section (upper part) is possible to appreciate the white matter arranged around a butterfly-shaped area of gray matter, together with spinal cord fibers entering the white matter. In the coronal section (lower part) a full reconstruction of the thoracic/lumbar area of the spinal cord can be appreciated. The vascularization (lower inset) is clearly visible along with the neuronal network (white spots).

cortex can be clearly resolved (right top inset).
In Fig.1b a 60 days old ALS affected mice (SOD1 model) spinal cord is shown. ALS is the most common and severe form of motor neuron diseases involving localized muscle weakness and respiratory symptoms. Superoxide dismutase 1 (SOD1) was the first identified ALS gene, upon which mouse models resembling ALS have been generated and extensively studied[5] .
In the spinal cord transverse section (Fig.1b, upper part) the white matter arranged around a butterfly-shaped area of gray matter, together with spinal cord fibers entering the white matter. In the coronal section (Fig.1b, lower part) a full reconstruction of the thoracic/lumbar area of the spinal cord can be appreciated. The vascularization (lower inset) is clearly visible along with the neuronal network (white spots).
The high resolution images obtained with Free-Space Propagation XPCT are very promising for the investigation of neurodegenerative diseases, even if it is not possible to quantify the densities and extract the chemical composition of the sample. Preliminary results to perform such measurements will be shown in the next paragraph.

2.2 Phase Imaging with the Hartmann sensor: basics and experimental results

The Hartmann wavefront sensor is a device capable to reconstruct independently the phase and amplitude of the incident beam with very high accuracy. A grid of regularly spaced holes is used to sample the wavefront, splitting the beam into beamlets that will result in an array of spots recorded by a 2D detector.
The main components of an Hartmann sensor are displayed in Fig.2. Inserting a sample before the Hartmann plate, will determine a shift of the spots at the detector plane (inset of Fig.2). An image of the Hartmann wavefront sensor, designed by Imagine Optic[15] , used for the experimental measurement can be seen on the right side of Fig.2.

The displacement Δx and Δy is proportional to the local slopes of the wavefront. It will produce a discrete map of the wavefront in the x and y directions that can be expressed in the following way:

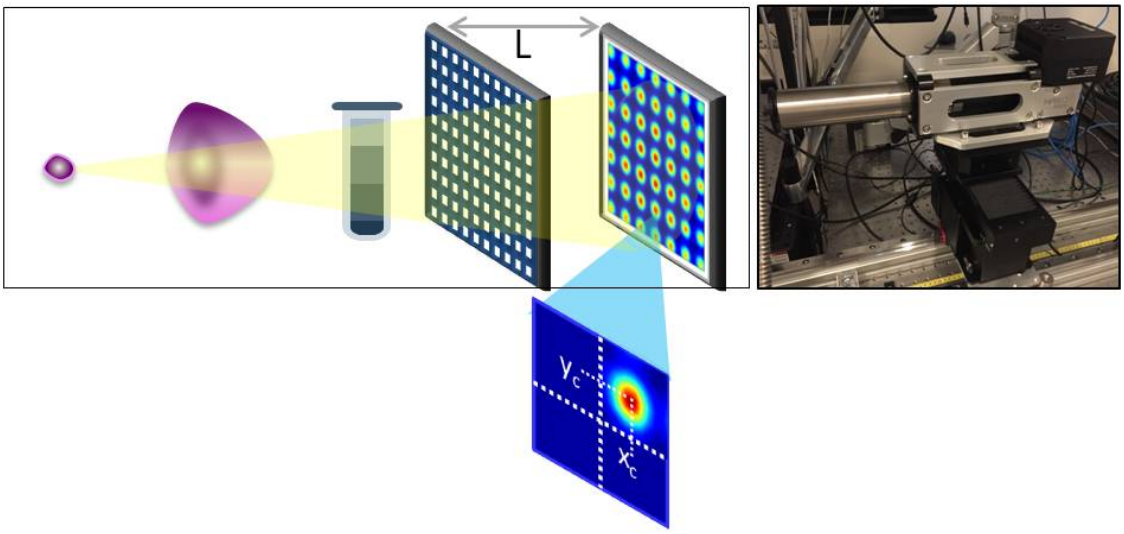

Figure 2. Left: Experimental set-up for the Hartmann sensor. The set-up is composed of : a source (point) , the incident wavefront (purple), the sample (gray), a Hartmann hole plate placed at a distance L from the detector. A magnification of the spot shift due to the presence of the sample is visible in the inset. Right: A picture of the Hartmann sensor utilized for the experimental part (designed by Imagine Optic[15]).

$$\begin{aligned} \frac{\partial \Phi(x_i, y_i)}{\partial x_i} &\approx \frac{\Delta x_{i,j}}{L} \\ \frac{\partial \Phi(x_i, y_i)}{\partial y_i} &\approx \frac{\Delta y_{i,j}}{L} \end{aligned} \tag{1}$$

where Φ is the wavefront, $\Delta x_{i,j}$ and $\Delta y_{i,j}$ are the measured shifts along the x and y directions of the spot of hole (i, j). L is the distance between the Hartmann plate and detection planes.
Measuring the local displacements (Δx, Δy) of the spots allows retrieving the local wave vectors (k_x and k_y). The integration of the k_x and k_y maps produces the wavefront map. Sample absorption can be also calculated integrating the signal correspondent to each hole and dividing it to the signal recorded without the sample. Therefore, a wavefront sensor generates the absorption and the phase maps of the sample[16] . The set-up described in Fig. 2 was used for a tomography experiment in collaboration with the company Imagine Optic. The source is the Excillum microfocus Metal-jet 70 kV, emitting a wide energy spectrum with an energy peak at 9 keV (Ga Kα). The goal is to perform a tomography experiment taking different materials as a target to reconstruct the absorption and the deflections resulting from the interaction with the objects. The samples are cylinder tubes made of carbon (1.5mm in diameter) or a tube of PMMA (2mm in diameter). The third is a 2mm diameter polycarbonate tube filled with 150 μm spheres of glass (Fig. 3). To reconstruct the sample in 3D, 400 tomographic projections are acquired under different viewing angles to cover 180°.
The coronal plane of the reconstructed absorption can be seen in Fig.3a ,while the reconstructed 3D deflection map can be seen in Fig.3b. The samples from left to right the tubes are Carbon, PMMA, and a tube filled with micro-spheres. The micro-spheres structure can be clearly seen in absorption (inset of Fig.3a), while some imperfections inside the PMMA can be only seen in the deflection map (inset of Fig.3b). The 3D reconstruction of the samples are shown in Fig.3c.

2.3 Simulation tool for Phase Imaging

As we have seen in the previous paragraphs, wavefront sensor provides the absorption and the phase maps of the sample. Moreover, 2D images are acquired from one acquisition making the measurement procedure fast and stable. Measurements can be performed with high sensitivity both with monochromatic or polychromatic beams since the system is lensless. The implementation of a real set-up for phase imaging with the Hartmann wavefront

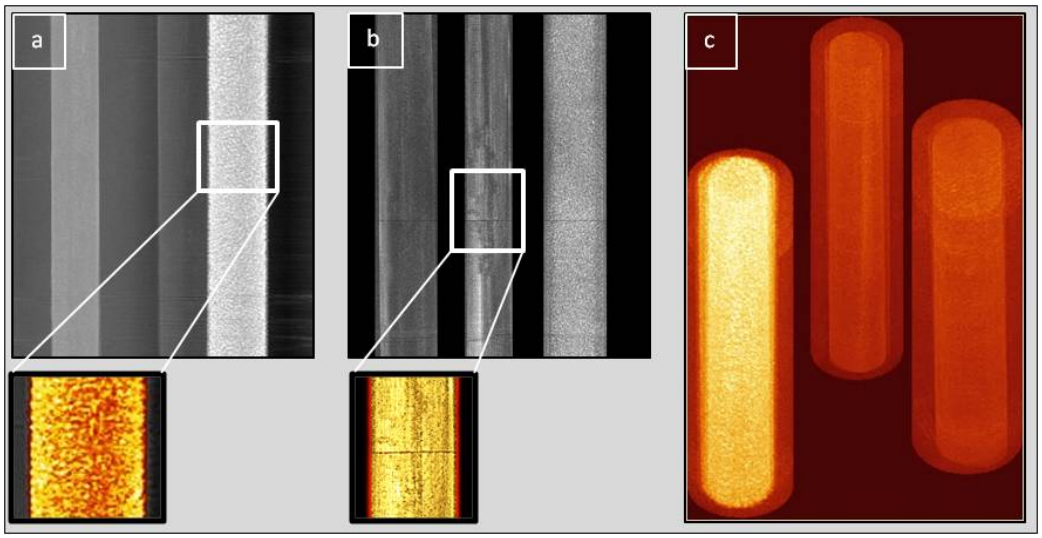

Figure 3. Tomographic images acquired with the Hartmann sensor in a cone beam configuration.From left to right: the samples are cylinder tubes made of carbon (1.5mm in diameter), a tube of PMMA (2mm in diameter, inset b)) and the third one is a 2mm diameter polycarbonate tube filled with 150 μm spheres of glass (inset a). The micro-spheres structure can be clearly seen in absorption (inset a)), while some imperfections inside the PMMA can be only seen in the deflection map (inset b). A 3D reconstruction of the samples is shown in c).

sensor can be challenging. In particular, the architecture of the Hartmann hole plate, the distances between the different elements of the set-up and the source properties are some of the crucial issues that determine the performances of the entire system.
A python simulation tool capable of giving the output of a real set-up has been implemented[17] .The source is designed as a superposition of Gaussian beams and thus can simulate any degree of coherence. Before the propagation each Gaussian beam is shifted in a random position chosen inside a larger Gaussian distribution (source size) and multiplied by a random phase factor.
In this way it is possible to simulate any sources from fully coherent to the incoherent (see also Sect. 3 and Sect. 4 [18].

For each optical element, the wavefront is calculated using Fresnel's propagators and the final electric field is given by the sum of the electric field of each Gaussian.
A simple sketch of the simulated set-up can be seen at the top of Fig.4, where z is the propagation distance, L is the screen dimension and U is the field at each plane. We show the results for the occurrence of diffraction and cross-talk between adjacent holes when changing the coherence of the illuminating beam. The degree of coherence was set inversely proportional to the number (N) of gaussians inside the source: N=1 Fig.4a, N=10 Fig.4b, N=1000 Fig.4c. Diffraction effects from the hole edges can be seen in the case of coherent illumination (Fig.4a), while for N=10 the displacement of the sub-sources associated to the interference of the propagated beams induces a strong change on the pattern (Fig.4b). Finally, in the case of strongly incoherent illumination (Fig.4c) a Gaussian shape for the diffraction pattern of each hole can be noticed.

ACKNOWLEDGMENTS

We would like to thank the support of Prematuration 2019 project from IP Paris. This research was funded by the 3DXlight project (European Union's Horizon 2020 research and innovation program) under grant agreement Nº 851956. This work has received funding from the European Union's Horizon 2020 research and innovation programme under grant agreement no 871124 Laserlab-Europe. This work was also funded by the Région Nouvelle-Aquitaine and the European Union FEDER under the XPULSE project (grant number n°3334910): "development of an imaging system using X-rays based on ultra-short intense laser for applications in breast

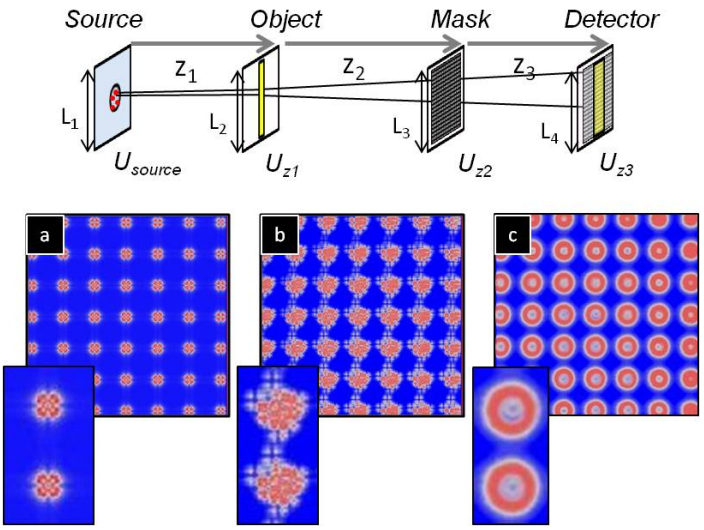

Figure 4. Top: Sketch of the simulated set-up, where z is the propagation distance, L is the screen dimension and U is the field at that plane. A series of images of the Hartmann mask are reported varying the degree of coherence of the incident beam. The degree of coherence was set proportionally to the number (N) of gaussians inside the source: N=1 a), N=10 b), N=1000 c). Diffraction effects from the hole edges can be seen in the case of coherent illumination a), the occurrence of cross-talk between adjacent holes is clear for partially coherent beam b), in the case of strongly incoherent illumination c) a Gaussian shape for the diffraction pattern of each hole can be noticed.

cancer imaging". The FISR Project 'Tecnopolo di nanotecnologia e fotonica per la medicina di precisione' (funded by MIUR/CNR, CUP B83B17000010001) and the TECNOMED project (funded by Regione Puglia, CUP B84I18000540002) are also acknowledged. We acknowledge Alphanov for giving us access to their X-ray source set-up. The authors acknowledge the help from collaborators from Imagine Optic in the data acquisition with the Hartmann sensor: Martin Piponnier and Laura Oudjedi.

REFERENCES

1. M. Fratini, I. Bukreeva, G. Campi, F. Brun, G. Tromba, P. Modregger, D. Bucci, G. Battaglia, R. Spadon, M. Mastrogiacomo, H. Requardt, F. Giove, A. Bravin, and A. Cedola, "Simultaneous submicrometric 3d imaging of the micro-vascular network and the neuronal system in a mouse spinal cord," 2014 , Sci Rep 5, 8514.
2. A. Olivo, S. E. Bohndiek, J. A. Griffiths, A. Konstantinidis, and R. D. Speller, "A non-free-space propagation x-ray phase contrast imaging method sensitive to phase effects in two directions simultaneously," *Applied Physics Letters* **94**, p. 044108, Jan. 2009.
3. E. Longo, A. Bravin, F. Brun, I. Bukreeva, A. Cedola, M. Fratini, X. Le Guevel, L. Massimi, L. Sancey, O. Tillement, P. Zeitoun, and O. de La Rochefoucauld, "3D map of theranostic nanoparticles distribution in mice brain and liver by means of X-ray Phase Contrast Tomography," *Journal of Instrumentation* **13**, p. C01049, Jan. 2018.
4. A. Bravin, P. Coan, and P. Suortti, "X-ray phase-contrast imaging: from pre-clinical applications towards clinics," *Physics in Medicine and Biology* **58**, p. R1, Jan. 2013.
5. G. Begani Provinciali, N. Pieroni, I. Bukreeva, M. Fratini, L. Massimi, L. Maugeri, F. Palermo, F. Bardelli, A. Mittone, A. Bravin, G. Gigli, F. Gentile, A. Fossaghi, N. Riva, A. Quattrini, and A. Cedola, "X-ray phase contrast tomography for the investigation of amyotrophic lateral sclerosis," *Journal of Synchrotron Radiation* **27**, pp. 1042–1048, Jul 2020.
6. A. Krol, *In-line Hard X-ray Holography for Biomedical Imaging.* 02 2011,Research andTechnologies, Prof. Joseph Rosen (Ed.), ISBN: 978-953-307-227-2, InTech.

7. I. Bukreeva, G. Campi, M. Fratini, R. Spanò, D. Bucci, G. Battaglia, F. Giove, A. Bravin, A. Uccelli, C. Venturi, M. Mastrogiacomo, and A. Cedola, "Quantitative 3d investigation of neuronal network in mouse spinal cord model," *Scientific Reports* **7**, p. 41054, 01 2017.
8. P. Cloetens, J. P. Guigay, C. D. Martino, J. Baruchel, and M. Schlenker, "Fractional talbot imaging of phase gratings with hard x rays," *Opt. Lett.* **22**, pp. 1059–1061, Jul 1997.
9. A. Momose, H. Takano, Y. Wu, K. Hashimoto, T. Samoto, M. Hoshino, Y. Seki, and T. Shinohara, "Recent progress in x-ray and neutron phase imaging with gratings," *Quantum Beam Science* **4**, p. 9, Feb 2020.
10. M. Langer, P. Cloetens, J.-P. Guigay, and F. Peyrin, "Quantitative comparison of direct phase retrieval algorithms in in-line phase tomography," *Medical Physics* **35**(10), pp. 4556–4566, 2008.
11. D. Paganin, S. C. Mayo, T. E. Gureyev, P. R. Miller, and S. W. Wilkins, "Simultaneous phase and amplitude extraction from a single defocused image of a homogeneous object," *Journal of Microscopy* **206**(1), pp. 33–40, 2002.
12. A. Cedola, A. Bravin, I. Bukreeva, M. Fratini, A. Pacureanu, A. Mittone, L. Massimi, P. Cloetens, P. Coan, G. Campi, R. Spanò, F. Brun, V. Grigoryev, V. Petrosino, C. Venturi, M. Mastrogiacomo, N. Kerlero de Rosbo, and A. Uccelli, "X-Ray Phase Contrast Tomography Reveals Early Vascular Alterations and Neuronal Loss in a Multiple Sclerosis Model," *Scientific Reports* **7**, p. 5890, July 2017.
13. L. Massimi, F. Brun, M. Fratini, I. Bukreeva, and A. Cedola, "An improved ring removal procedure for in-line x-ray phase contrast tomography," *Physics in Medicine & Biology* **63**, p. 045007, feb 2018.
14. L. Massimi, I. Bukreeva, G. Santamaria, M. Fratini, A. Corbelli, F. Brun, S. Fumagalli, L. Maugeri, A. Pacureanu, P. Cloetens, N. Pieroni, F. Fiordaliso, G. Forloni, A. Uccelli, N. Kerlero de Rosbo, C. Balducci, and A. Cedola, "Exploring alzheimer's disease mouse brain through x-ray phase contrast tomography: From the cell to the organ," *NeuroImage* **184**, pp. 490 – 495, 2019.
15. O. de La Rochefoucauld, S. Bucourt, D. Cocco, G. Dovillaire, F. Harms, M. Idir, D. Korn, X. Levecq, M. Piponnier, R. Rungsawang, and P. Zeitoun, "Hartmann wavefront sensor in the EUV and hard X-ray range for source metrology and beamline optimization (Conference Presentation)," in *Relativistic Plasma Waves and Particle Beams as Coherent and Incoherent Radiation Sources III*, D. A. Jaroszynski and M. Hur, eds., **11036**, International Society for Optics and Photonics, SPIE, 2019.
16. O. de La Rochefoucauld, G. Dovillaire, F. Harms, M. Idir, L. Huang, X. Levecq, M. Piponnier, and P. Zeitoun, "EUV and Hard X-ray Hartmann wavefront sensing for optical metrology, alignment and phase imaging," *Submitted to Sensors* .
17. G. B. Provinciali, A. Cedola, O. de La Rochefoucauld, and P. Zeitoun, "Modelling of phase contrast imaging with x-ray wavefront sensor and partial coherence beams," *Sensors* **20**, p. 6469, Nov 2020.
18. D. Bleiner, The Science and Technology of X-ray Lasers: A 2020 Update Proc. SPIE 11886, 1188602 (2021)